

Mining S-PLUS for Metal-Poor Stars in the Milky Way

2 VINICIUS M. PLACCO ,¹ FELIPE ALMEIDA-FERNANDES ,^{1,2} ANKE ARENTSEN ,³ YOUNG SUN LEE,⁴
3 WILLIAM SCHOENELL ,⁵ TIAGO RIBEIRO,⁶ ANTONIO KANAAN,⁷ AND CLÁUDIA MENDES DE OLIVEIRA²

4 ¹ NSF's NOIRLab, 950 N. Cherry Ave., Tucson, AZ 85719, USA

5 ² Departamento de Astronomia, Instituto de Astronomia, Geofísica e Ciências Atmosféricas da USP, Cidade
6 Universitária, 05508-900, São Paulo, SP, Brazil

7 ³ Université de Strasbourg, CNRS, Observatoire Astronomique de Strasbourg, UMR 7550, F-67000 Strasbourg, France

8 ⁴ Department of Astronomy and Space Science, Chungnam National University, Daejeon 34134, South Korea

9 ⁵ GMTO Corporation 465 N. Halstead Street, Suite 250 Pasadena, CA 91107, USA

10 ⁶ Rubin Observatory Project Office, 950 N. Cherry Ave., Tucson, AZ 85719, USA

11 ⁷ Departamento de Física, Universidade Federal de Santa Catarina, Florianópolis, SC 88040-900, Brazil

ABSTRACT

This work presents the medium-resolution ($R \sim 1,500$) spectroscopic follow-up of 492 low-metallicity star candidates from the Southern Photometric Local Universe Survey (S-PLUS). The objects were selected from narrow-band photometry, taking advantage of the metallicity-sensitive S-PLUS colors. The follow-up observations were conducted with the Blanco and Gemini South Telescopes, using the COSMOS and GMOS spectrographs, respectively. The stellar atmospheric parameters (T_{eff} , $\log g$, and $[\text{Fe}/\text{H}]$), as well as carbon and α -element abundances, were calculated for the program stars, in order to assess the efficacy of the color selection. Results show that $92^{+2}_{-3}\%$ of the observed stars have $[\text{Fe}/\text{H}] \leq -1.0$, $82^{+3}_{-4}\%$ have $[\text{Fe}/\text{H}] \leq -2.0$, and $14^{+3}_{-3}\%$ have $[\text{Fe}/\text{H}] \leq -3.0$, including one ultra metal-poor star ($[\text{Fe}/\text{H}] \leq -4.0$). The sample also includes 59 Carbon-Enhanced Metal-Poor stars, with 4 stars belonging to Group-III. Based on the calculated metallicities, further S-PLUS color cuts are proposed, which can increase the fractions of stars with $[\text{Fe}/\text{H}] \leq -1.0$ and ≤ -2.0 to 98% and 88%, respectively. Such high success rates enable targetted high-resolution spectroscopic follow-up efforts, as well as provide selection criteria for fiber-fed multiplex spectroscopic surveys.

Keywords: Narrow band photometry (1088), Metallicity (1031), Stellar atmospheres (1584), Chemical abundances (224)

1. INTRODUCTION

There is a wealth of information contained in the colors of stars (Allende Prieto 2016), which are simply the difference in integrated fluxes on two given photometric bandpasses. The first determinations of effective temperatures from photometry date back to the early 20th century (Greaves et al. 1929) and since then extensive work has been conducted to characterize and calibrate temperature scales in optical (Bessell 1979) and near-infrared (Alonso et al. 1996, 1999; Casagrande et al. 2010) systems, just to mention a few. The same applies

to estimating the metallicity ($[\text{Fe}/\text{H}]^1$) of stellar sources from photometry. Many studies in the literature relied on the calibration of the ultra-violet excess for stellar sources, which is heavily dependent on the metallicity (Wallerstein 1964; Schuster & Nissen 1989; Bonifacio et al. 2000), but there are others that take advantage of infrared colors, depending on the stellar population (e.g. cold brown dwarfs - Leggett et al. 2010).

More recently, large scale surveys have taken these photometric parameter determination strategies to the next level, by building databases with millions of spectroscopically-observed objects. Two such examples

Corresponding author: Vinicius M. Placco
vinicius.placco@noirlab.edu

¹ $[\text{A}/\text{B}] = \log(N_A/N_B)_* - \log(N_A/N_B)_{\odot}$, where N is the number density of atoms of a given element in the star ($*$) and the Sun (\odot), respectively.

are the Sloan Digital Sky Survey (SDSS; York et al. 2000) in the northern hemisphere and the SkyMapper Sky Survey (SMSS; Wolf et al. 2018) in the southern hemisphere. Both of these surveys conducted separate sub-surveys aiming to perform medium-resolution ($R \sim 1,500$) spectroscopic follow-up of stars in the Milky Way Galaxy: the Sloan Extension for Galactic Understanding and Exploration (SEGUE-1; Yanny et al. 2009) and SEGUE-2 (Rockosi et al. 2022), and the AAOmega Evolution of Galactic Structure (AEGIS; Keller et al. 2007; Yoon et al. 2018, among others). These not only served as the basis for a number of statistical studies of stellar populations in the Milky Way, but also as prime datasets for high-resolution spectroscopic follow-up and calibration of photometric parameter determinations.

The SDSS makes use of the Sloan Photometric System, which comprises of five colors ($u'/g'/r'/i'/z'$) that cover the region between 3,000 Å and 11,000 Å into five essentially nonoverlapping passbands (Fukugita et al. 1996). Ivezić et al. (2008) were able to determine temperatures (with typical uncertainties of ~ 100 K) and metallicities (with uncertainties of 0.2 dex or better for $-2.0 \leq [\text{Fe}/\text{H}] \leq -0.5$) for over 2 million F/G stars in the Milky Way. One of the limitations on the low-metallicity end is due to the broadness of the u filter, which loses its metallicity sensitivity, hampering efforts to extend the determinations to $[\text{Fe}/\text{H}] \leq -2.5$. In two follow-up studies from the work of Ivezić et al. (2008), An et al. (2013) and An et al. (2015) re-determined the photometric metallicities and the metallicity distribution functions (MDFs) in the Galactic halo from SDSS photometry. These efforts relied on improved photometry from the Stripe 82 region of SDSS and were able to increase the metallicity range of the photometric estimates down to $[\text{Fe}/\text{H}] \sim -2.5$.

The SkyMapper filter set design was optimized for stellar astrophysics, in particular the study of stellar populations in the Milky Way (Keller et al. 2007). It is composed of six filters: $u/v/g/r/i/z$ (Bessell et al. 2011). The u ($\lambda_{\text{cen}} = 349$ nm) and v ($\lambda_{\text{cen}} = 384$ nm) filters are a two-filter version of the SDSS u' , providing additional photometric sensitivity. The SkyMapper Data Release 1 (DR1; Wolf et al. 2018) has been extensively used to determine photometric stellar atmospheric parameters and select low-metallicity stars for spectroscopic follow-up. Casagrande et al. (2019), using the SkyMapper DR1, were able to determine temperatures and metallicities with uncertainties better than ~ 100 K and ~ 0.2 dex for $[\text{Fe}/\text{H}] \geq -2.0$, respectively. A similar study by Huang et al. (2019), limited to red giant stars, were able to reach slightly lower uncertainties (~ 80 K and ~ 0.18 dex), however with the parameter space still

limited to $[\text{Fe}/\text{H}] \geq -2.0$, with only a few objects with metallicities below this threshold. Chiti et al. (2021a) extended the low-metallicity limit to $[\text{Fe}/\text{H}] < -2.5$ with $\sigma \sim 0.31$ dex, with the goal of constructing the photometric MDF of the Milky Way (Chiti et al. 2021b). In terms of spectroscopic follow-up, Da Costa et al. (2019) presents 2,618 candidates selected to have photometric $[\text{Fe}/\text{H}] < -2.0$ from their metallicity-sensitive diagram. Results show that over 40% of the observed stars have $[\text{Fe}/\text{H}] \leq -2.75$.

The Pristine Survey (Starkenburg et al. 2017) has been successfully using narrow-band photometry on the metallicity sensitive Ca II H and K absorption features (in addition to SDSS broad-band g and i) to search for low-metallicity stars in the Galaxy from the Northern hemisphere. The ~ 100 Å wide narrow-band filter has a larger predictive power than the broader band counterparts of SDSS and SkyMapper and is able to successfully predict metallicities in the $[\text{Fe}/\text{H}] \sim -3.0$ regime (Youakim et al. 2017). The results of a three-year medium-resolution spectroscopic follow-up campaign show that $\sim 70\%$ of the 1,007 stars observed have $[\text{Fe}/\text{H}] < -2.0$ and $\sim 9\%$ have $[\text{Fe}/\text{H}] < -3.0$ (Aguado et al. 2019)².

The Javalambre Photometric Local Universe Survey (J-PLUS; Cenarro et al. 2019) and the Southern Photometric Local Universe Survey (S-PLUS; Mendes de Oliveira et al. 2019) have a unique 12 broad- and narrow-band filter set, consisting of four SDSS (g, r, i, z), one modified SDSS u , and seven narrow-band filters. The narrow-band filters were designed to probe very specific regions in the optical wavelength regime and accommodate a wide variety of science cases, from high-precision photometric redshifts (Molino et al. 2019) to the identification of low-metallicity stars in the Galactic halo (Andrés Galarza et al. 2021). The names and key absorption features sampled by the narrow-band filters are: $J0378 - [\text{O II}]$; $J0395 - \text{Ca II H+K}$; $J0410 - \text{H}\delta$; $J0430 - G$ band; $J0515 - \text{Mg } b$ triplet; $J0660 - \text{H}\alpha$; and $J0861 - \text{Ca}$ triplet. It is worth pointing out that the $J0395$ filter shares a similar central wavelength and width as the Pristine narrow-band filter. However, J-PLUS and S-PLUS have the advantage of also performing narrow band photometry in the Mg b triplet ($J0515$) and Ca ($J0861$) triplet regions, which are also useful for metallicity and surface gravity determinations (Majewski et al. 2000). Whitten et al. (2019) used J-PLUS

² The Pristine Survey has individual photometric metallicities to compare to the spectroscopic determinations. For the work of Aguado et al. 2019, 23% of the stars with photometric $[\text{Fe}/\text{H}] < -3.0$ also have spectroscopic $[\text{Fe}/\text{H}] < -3.0$.

photometry to predict T_{eff} and [Fe/H] using artificial neural networks and reached uncertainties of ~ 91 K and ~ 0.25 dex for stars in the $-3.0 \lesssim [\text{Fe}/\text{H}] \leq -0.5$. In a follow-up study using S-PLUS, Whitten et al. (2021) were able to estimate the first photometric carbon abundances for a sample of over 50,000 stars, with uncertainties better than ~ 0.35 dex.

The possibility of accurately determining stellar atmospheric parameters and chemical abundances for large datasets drawn from photometry, and especially for a wide range of metallicities, is fundamental in the context of studying low-metallicity stars. Very Metal-Poor (VMP - $[\text{Fe}/\text{H}] < -2.0$; Beers & Christlieb 2005) stars are the “local” observational probes that allow astronomers to address questions at cosmological scales (Bromm & Larson 2004). The research that was once limited to individual stars (Carney & Peterson 1981) has been expanded to much larger samples, allowing the investigation of relations such as the carbon-enhancement observed in metal-poor stars (Lucatello et al. 2006; Aoki et al. 2007), the possible origins of the subclasses within this group (Masseron et al. 2010), and their role in the chemical evolution of the early universe (Woosley & Weaver 1995; Heger & Woosley 2002; Meynet et al. 2006; Norris et al. 2013; Frebel & Norris 2015). Growing statistics on VMP stars narrow error bars and broadens our understanding of the early stages of the chemical evolution of the Universe.

This article reports on the medium-resolution ($R \sim 1,500$) spectroscopic follow-up of low-metallicity star candidates selected from the S-PLUS Data Release 3 (DR3). The main goal is to assess whether the metallicity-sensitive S-PLUS colors are effective in selecting metal-poor stars for spectroscopic follow-up. Section 2 describes the medium-resolution spectroscopic observations, followed by the estimates of the stellar atmospheric parameters and abundances in Section 3. We analyze the sensitivity of the narrow-band photometry to the stellar parameters, as well as the effectiveness of the S-PLUS color selection for low-metallicity stars in Section 4. Our conclusions and prospects for future work are provided in Section 5.

2. TARGET SELECTION AND OBSERVATIONS

2.1. The S-PLUS Data Release 3

For this work, the S-PLUS Data Release 3 (DR3; Buzzo et al., in prep) was used. The data structure in this data release, as well as the photometric extraction and calibration process, are the same as the S-PLUS Data Release 2 (DR2; Almeida-Fernandes et al. 2022). The only difference is the addition of observations in the South Galactic Hemisphere for DR3. At the time

the candidates for this work were selected, the catalogs were only available internally to the collaboration and are now publicly available through the S-PLUS Cloud³ service.

The first step in the data selection was to apply a series of restrictions in the DR3 database, mostly related to the quality of the photometry, probability of being a stellar source, and a color range suitable to study low-metallicity stars. Then, metal-poor star candidates were chosen for the medium-resolution spectroscopic campaign, based on their location on a metallicity-dependent color-color diagram, as described below. The following restrictions were applied to the DR3 database:

- $\text{CLASS_STAR} \geq 0.95$: sources having a high probability of being a star;
- $\text{gSDSS} \leq 17.5$: brightness limit for spectroscopic follow-up within reasonable exposure times;
- $\text{nDet_magPStotal} = 12$: only sources with all twelve magnitudes measured;
- $(\text{gSDSS}-\text{iSDSS}) \in [0.2:1.6]$: color window to remove possible contamination from white dwarfs and A-type stars on the blue end and objects cooler than $T_{\text{eff}} \sim 4000$ K on the red end;
- $(\text{J0410}-\text{J0861}) \in [0.3:3.5]$: same as above using a narrow-band color;
- **Total:** 820,829 stars.

The S-PLUS magnitudes used throughout this work are the 3-arcsec aperture corrected values, labelled PStotal . The left panel of Figure 1 shows the density of the selected stars in a color-color diagram. The color $(\text{J0395}-\text{J0660})-2\times(\text{g}-\text{i})$ was chosen based on the work of Starkenburg et al. (2017) for the Pristine Survey, which is proven to have a strong $[\text{Fe}/\text{H}]$ -dependency. The g filter was replaced with J0660 as a temperature sensitive feature and the $-2\times(\text{g}-\text{i})$ was used to re-shape the color-color diagram. In the x-axis, both Starkenburg et al. (2017) and Da Costa et al. (2019) employ the $(\text{g}-\text{i})_0$ color. Due to the dependency of the Ca II K line strength with temperature, there is a color range, roughly $(\text{g}-\text{i})_0 \lesssim 0.3$, where the metallicity-dependent color difference between a star with $[\text{Fe}/\text{H}] = -2.0$ and -4.0 becomes smaller than the typical uncertainties in the photometry. In an attempt to address this degeneracy, this work employs the $(\text{J0395}-\text{J0410})-(\text{J0660}-\text{J0861})$ combination, that uses the filters centered on $\text{H}\delta$ and $\text{H}\alpha$ and provides better temperature sensitivity. This temperature-dependent

³ <https://splus.cloud/>

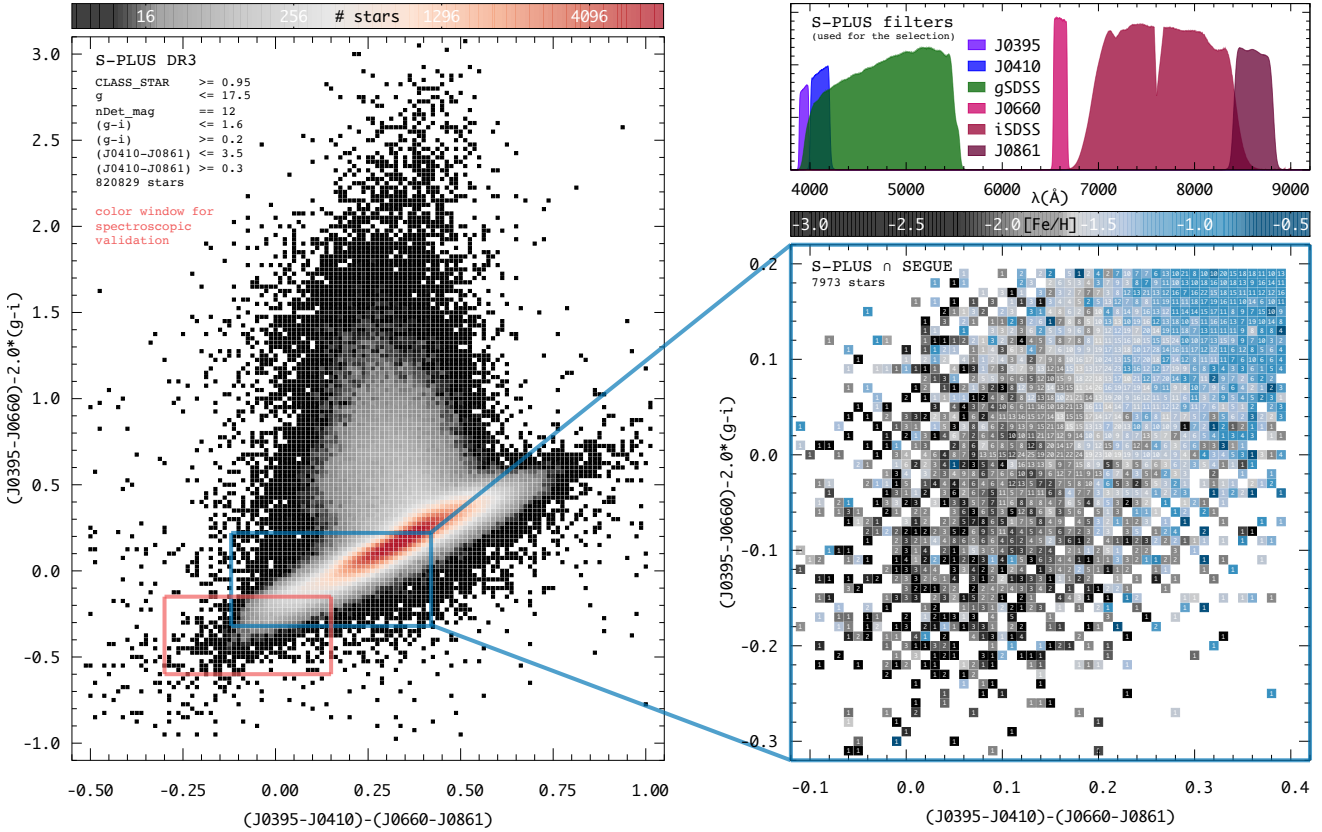


Figure 1. Left panel: stellar density for the selected S-PLUS DR3 sample in a color-color diagram. The red box outlines the color window for the spectroscopic follow-up (see text for details). The inset (bottom right panel) shows the cross-match with the SDSS/SEGUE spectroscopic database, color-coded by the average metallicity in each bin. The number of stars in each bin is also shown. Top right panel: S-PLUS transmission curves for the six narrow-band and broad band filters used in this selection.

metallicity color index should increase the success rate of finding metal-poor stars. The transmission curves for the six S-PLUS filters used in this selection are shown in the top right panel of Figure 1.

The catalog generated from the S-PLUS DR3 selection above was cross-matched with the SDSS/SEGUE spectroscopic database. From that cross-match, sources with $\text{CLASS} == \text{QSO}$, $\sigma_{\text{Teff}} > 200 \text{ K}$, and $\text{S/N} < 20$ were excluded. The lower right panel of Figure 1 shows a section of the color-color diagram, with each 0.01×0.01 bin colored by its average $[\text{Fe}/\text{H}]$ value from the spectroscopic data. Also shown in each bin are the number of stars used to calculate the average. The metallicity dependency is very evident in both axes and allows for an improved selection of potential metal-poor stars for spectroscopic follow-up.

Figure 2 further explores this color space. Each panel shows a different metallicity regime, color coded by the fraction of stars in each 0.05×0.05 bin. The number of stars in each bin is also shown. As an example, the bin centered on $(0.0, -0.1)$ has 1 star with $[\text{Fe}/\text{H}] > -1.0$ ($\sim 2\%$), 19 stars with $-2.0 < [\text{Fe}/\text{H}] \leq -1.0$ ($\sim 46\%$), and 21 stars with $[\text{Fe}/\text{H}] \leq -2.0$ ($\sim 52\%$). For the

spectroscopic follow-up, from the right panel, a cut was made where most bins have at least a 50% fraction of $[\text{Fe}/\text{H}] \leq -2.0$ star. Limits were also placed on the blue end of each color, to avoid sources with potentially spurious colors. The final color window for the selection of targets for the spectroscopic follow-up was defined as: $(\text{J0395}-\text{J0410})-(\text{J0660}-\text{J0861}) \in [-0.30:0.15]$ and $(\text{J0395}-\text{J0660})-2 \times (g-i) \in [-0.60:-0.15]$ (see red-colored box in the left panel of Figure 1). Within this window, targets were chosen based on their brightness and observability at a given telescope. Details are provided in the next section.

2.2. Medium-Resolution Spectroscopy

The spectroscopic follow-up campaign was conducted in semesters 2019A, 2019B, 2020A, 2021A, and 2022A. Data were collected for 492 metal-poor star candidates, selected from their S-PLUS photometry, described above. The stars were observed with two different telescope/instrument setups: Blanco/COSMOS and Gemini South/GMOS-S.

The distribution (in Galactic coordinates) of the observed stars is shown in the top panel of Figure 3, color-

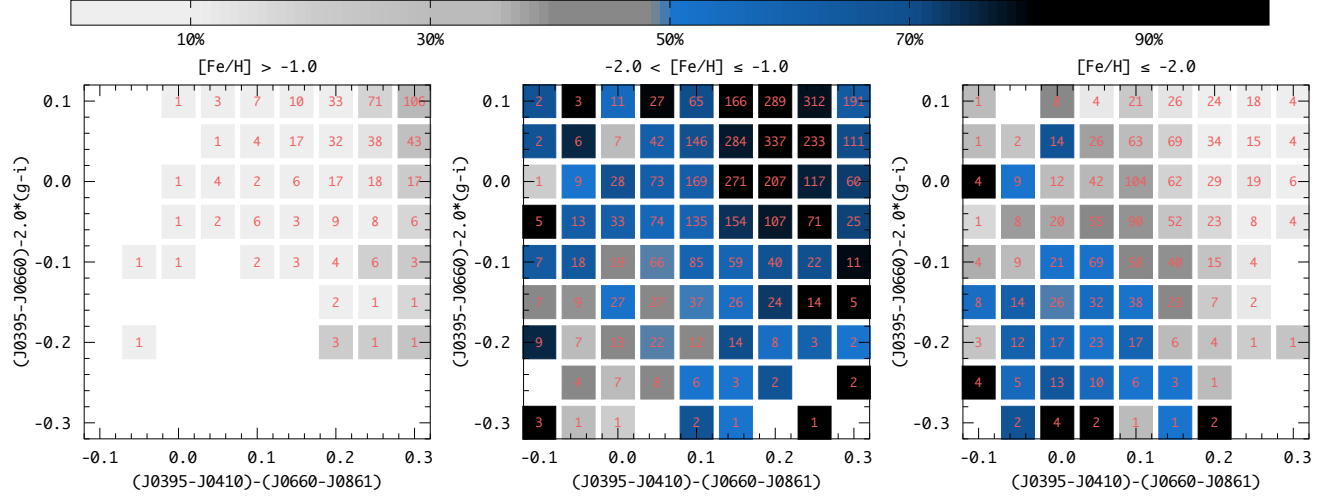


Figure 2. Color-color diagram for three different $[\text{Fe}/\text{H}]$ regimes. The bins in each panel are color-coded by the fraction of stars with an average metallicity in a given range. The number of stars in each bin is also shown.

293 coded by telescope. The point size is proportional to the
 294 g magnitude of each target. The dust map traces the
 295 Galactic plane and was constructed from the Schlegel
 296 et al. (1998) reddening values. Also shown (gray solid
 297 line) is the celestial equator. The apparent grouping of
 298 the stars is due to the S-PLUS observing strategy, which
 299 started with the STRIPE82 (equatorial) region (DR1),
 300 then moving towards halo fields at lower southern de-
 301 clinations (DR2 and DR3). Note that most of the faint
 302 targets were observed with the Gemini telescope, due to
 303 its larger aperture. Table 1 lists the name, coordinates,
 304 and observing details for each star. The bottom panels
 305 of Figure 3 show the magnitude distribution of the ob-
 306 served targets in all the 12 S-PLUS filters. Each panel
 307 displays the transmission curve for the filters with their
 308 central wavelength (in Å). Table 2 lists all the magni-
 309 tude values (and errors) for the observed stars, taken
 310 from the S-PLUS DR3 catalog.

311 For consistency in the spectroscopic observations,
 312 grating/slit combinations were chosen to yield a resolv-
 313 ing power $R \sim 1,200 - 1,800$, and exposure times were
 314 set to reach a signal-to-noise ratio of at least $\text{S/N} \sim 30$
 315 per pixel at the Ca II K line (3933.3 Å). Calibration
 316 frames included arc-lamp exposures, bias frames, and
 317 quartz flats. Specific details of each instrument and data
 318 reduction are given below.

319 *CTIO Blanco Telescope*—A total of 384 stars were ob-
 320 served with the Víctor M. Blanco 4-meter Telescope,
 321 located at the Cerro Tololo Inter American Observa-
 322 tory, using the COSMOS (Cerro Tololo Ohio State
 323 Multi-Object Spectrograph; Martini et al. 2014) instru-
 324 ment. Observations were conducted in remote visitor
 325 mode in October 2019, December 2020, January 2021,
 326 and April 2022 (2019B-0069, 2020A-0032, and 2022A-

327 210002). The exposure times ranged from 90 to 1800
 328 seconds, with a total of 57.96 hours on target. The
 329 setup included a 600 l mm^{-1} grating (blue setting)
 330 and a $1''.5$ slit, resulting in a wavelength coverage in
 331 the range $[3600:6300]$ Å at resolving power $R \sim 1,800$.
 332 All tasks related to spectral reduction, extraction, and
 333 wavelength calibration were performed using standard
 334 IRAF⁴ packages.

335 *Gemini South Telescope*—108 stars were observed with
 336 the 8.1 m Gemini South telescope and the GMOS (Gem-
 337 ini Multi-Object Spectrographs; Davies et al. 1997; Gi-
 338 meno et al. 2016) instrument. Observations were con-
 339 ducted in the “Poor Weather” queue mode in April-June
 340 2019 and June-July 2021 (GS-2019A-Q-408 and 2021A-
 341 Q-419). The exposure times ranged from 210 to 1800
 342 seconds, with a total of 33.26 hours on target. The
 343 $B600 \text{ l mm}^{-1}$ grating (G5323) and a $1''.5$ slit were used
 344 with a 2×2 binning, resulting in a wavelength coverage
 345 in the range $[3200:5800]$ Å at resolving power $R \sim 1,200$.
 346 The complete data reduction was performed using the
 347 DRAGONS⁵ software package (Labrie et al. 2019).

3. STELLAR PARAMETERS AND CHEMICAL ABUNDANCES

350 The determinations of stellar atmospheric parameters
 351 (T_{eff} , $\log g$, and $[\text{Fe}/\text{H}]$), carbonicity ($[\text{C}/\text{Fe}]$), and α -
 352 to-iron ratios ($[\alpha/\text{Fe}]$) for the stars observed as part of
 353 spectroscopic follow-up were made using the n-SSPP
 354 (Beers et al. 2014, 2017), which is a modified version
 355 of the SEGUE Stellar Parameter Pipeline (SSPP; Lee

⁴ <https://iraf-community.github.io/>.

⁵ <https://github.com/GeminiDRSoftware/DRAGONS>.

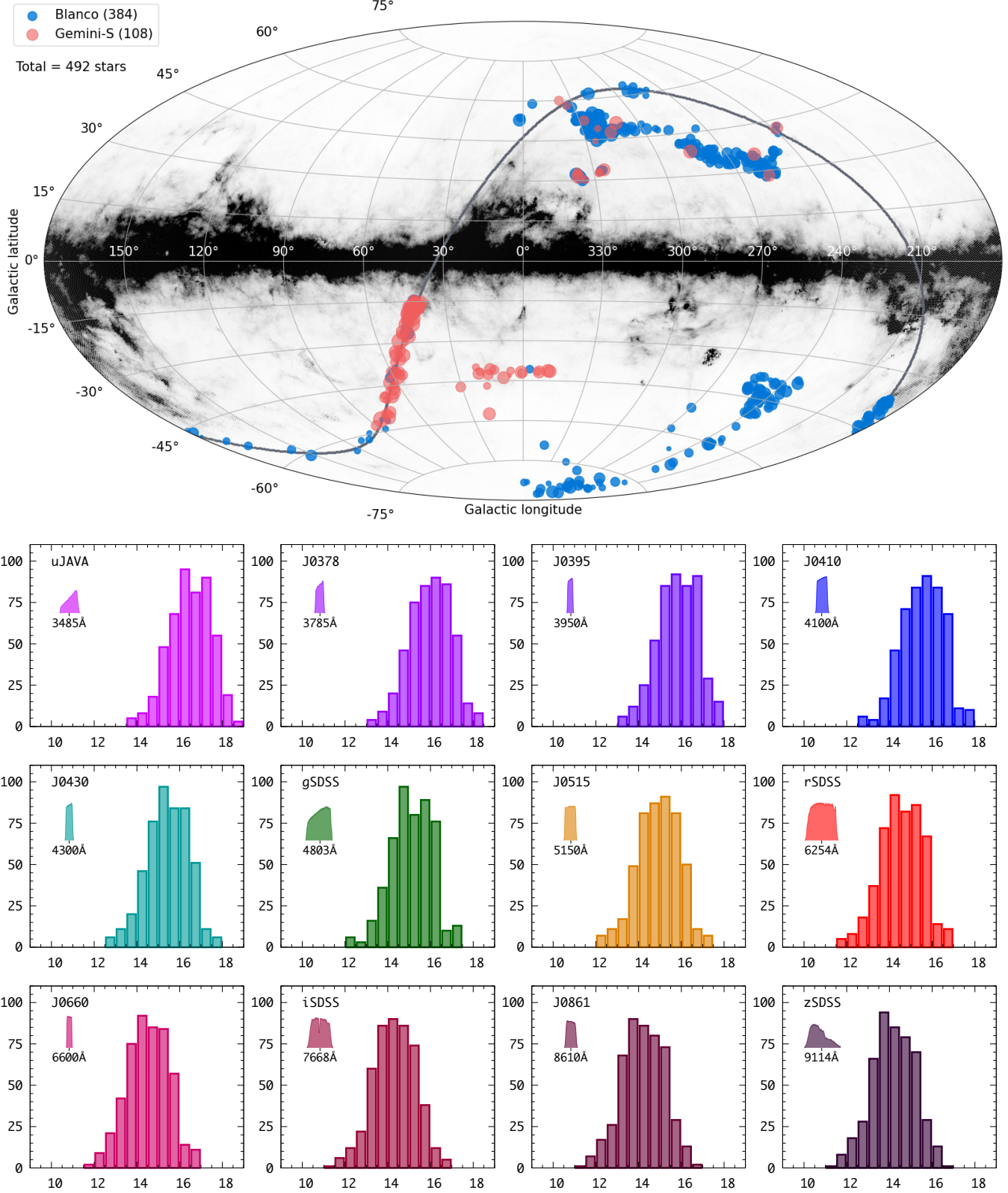


Figure 3. Top: Galactic coordinates for the stars observed in this work, color-coded by telescope. The point size is proportional to the g magnitude. The gray line traces the celestial equator. The dust map uses reddening values from Schlegel et al. (1998). Bottom: Magnitude distribution of the observed stars in the 12-filter system of S-PLUS. Each panel also shows the name, transmission curve, and central wavelength (in Å) for the filters.

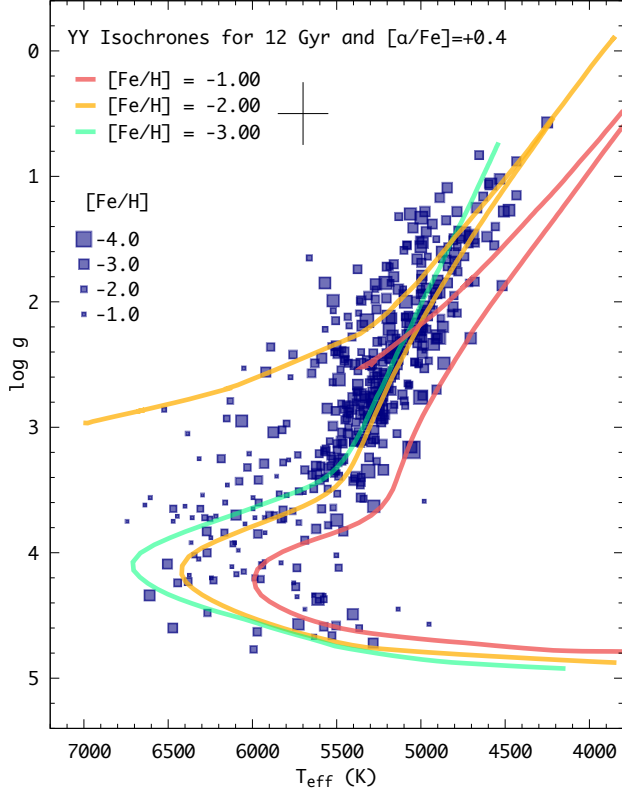


Figure 4. Surface gravity vs. T_{eff} diagram for the program stars, using the parameters calculated by the n-SSPP, listed in Table 3. The point size is inversely proportional to the metallicity. Also shown are the YY Isochrones (12 Gyr, $0.8 M_{\odot}$, $[\alpha/\text{Fe}] = +0.4$; Demarque et al. 2004) for $[\text{Fe}/\text{H}] = -1.0$, -2.0 , and -3.0 , and horizontal-branch tracks from Dotter et al. (2008).

et al. 2008a,b, 2011, 2013). The software uses photometric and spectroscopic information to calculate the atmospheric parameters based on spectral line indices, photometric calibrations, and synthetic spectra matching. The $[\text{C}/\text{Fe}]$ and $[\alpha/\text{Fe}]$ are estimated from the strength of the CH G-band molecular feature at $\sim 4300 \text{ \AA}$ and the Mg I triplet at $5150\text{--}5200 \text{ \AA}$, respectively. The n-SSPP was able to estimate T_{eff} , $\log g$, and $[\text{Fe}/\text{H}]$ for all the 492 stars observed as part of this work. The $[\text{C}/\text{Fe}]$ and $[\alpha/\text{Fe}]$ abundance ratios were estimated for 429⁶ and 464 stars, respectively. The average uncertainties for this sample are 70 K for T_{eff} , 0.24 dex for $\log g$, 0.11 dex for $[\text{Fe}/\text{H}]$, and 0.21 dex for $[\text{C}/\text{Fe}]$ and $[\alpha/\text{Fe}]$.

The adopted atmospheric parameters and abundance ratios for the sample are listed in Table 3. Also in-

⁶ Most stars without carbon abundance determinations were observed with CTIO/Blanco. There was an artifact at the exact same position as the CH band head that affected some of the spectra and prevented reliable spectral fits by the n-SSPP.

cluded in the table are the corrections for carbon abundances, based on the stellar-evolution models presented in Placco et al. (2014), the final $[\text{C}/\text{Fe}]$, and $A(\text{C})$ ⁷, the latter two including the corrections. Figure 4 shows the $\log g$ vs. T_{eff} diagram for the sample, compared with the YY isochrones for different metallicities (12 Gyr, $0.8 M_{\odot}$, $[\alpha/\text{Fe}] = +0.4$; Demarque et al. 2004). The point sizes are inversely proportional to the $[\text{Fe}/\text{H}]$ values and typical uncertainties are also shown. Based on the color selection from the S-PLUS filters, it is expected that the majority of the stars ($\sim 78\%$) have temperatures in the $[4700:5700]$ K range. There is an overall agreement between observations and the isochrones for $[\text{Fe}/\text{H}] = -2.0$ and -3.0 , apart from a small systematic offset of $\sim 50 - 100$ K for the spectroscopic temperatures. In addition, it is evident that the majority of the higher metallicity stars (smaller symbols, in particular $[\text{Fe}/\text{H}] \geq -1.0$, have $T_{\text{eff}} \geq 5700$ K. This will be further discussed in Section 4.4.

Figure 5 shows example spectra for the 100 most metal-poor stars observed with Blanco (left panel) and Gemini-South (right panel), which have both $[\text{C}/\text{Fe}]$ and $[\alpha/\text{Fe}]$ determined by the n-SSPP. Also shown are the adopted parameters for each target (see Section 3 for details). The absorption features of interest for the calculation of each parameter are identified on the top of the panels. The shaded regions correspond to the specific atmospheric parameter or chemical abundance probed by the S-PLUS filters outlined on the bottom of the panels. The spectra are sorted by $[\text{Fe}/\text{H}]$. Despite the variation in T_{eff} , it is possible to note the overall decrease in the strength of the Ca II features as the metallicity decreases, as well as the increase in T_{eff} , $A(\text{C})$, and $[\alpha/\text{Fe}]$ as their associated absorption features strengthen.

4. ANALYSIS AND DISCUSSION

4.1. $[\text{Fe}/\text{H}]$ sensitivity from narrow-band photometry

As described in Section 2, the S-PLUS colors using the narrow-band J0395 filter are effective in separating different metallicity regimes (see also Figure 2). Hence, for a given temperature, the difference between the J0395 and J0660 magnitudes should decrease as a function of $[\text{Fe}/\text{H}]$ ⁸. An attempt to illustrate and quantify this effect is shown in Figure 6. There are two sets of Spectral Energy Distributions (SED) with ten stars each, in two narrow temperature intervals. The magnitudes were scaled to an arbitrary zSDSS value in order to preserve

⁷ $A(\text{C}) = \log(N_C/N_H) + 12$

⁸ As an example, for two stars with the same $T_{\text{eff}}/\log g$ and at the same distance, the one with the lowest metallicity would be brighter in J0395.

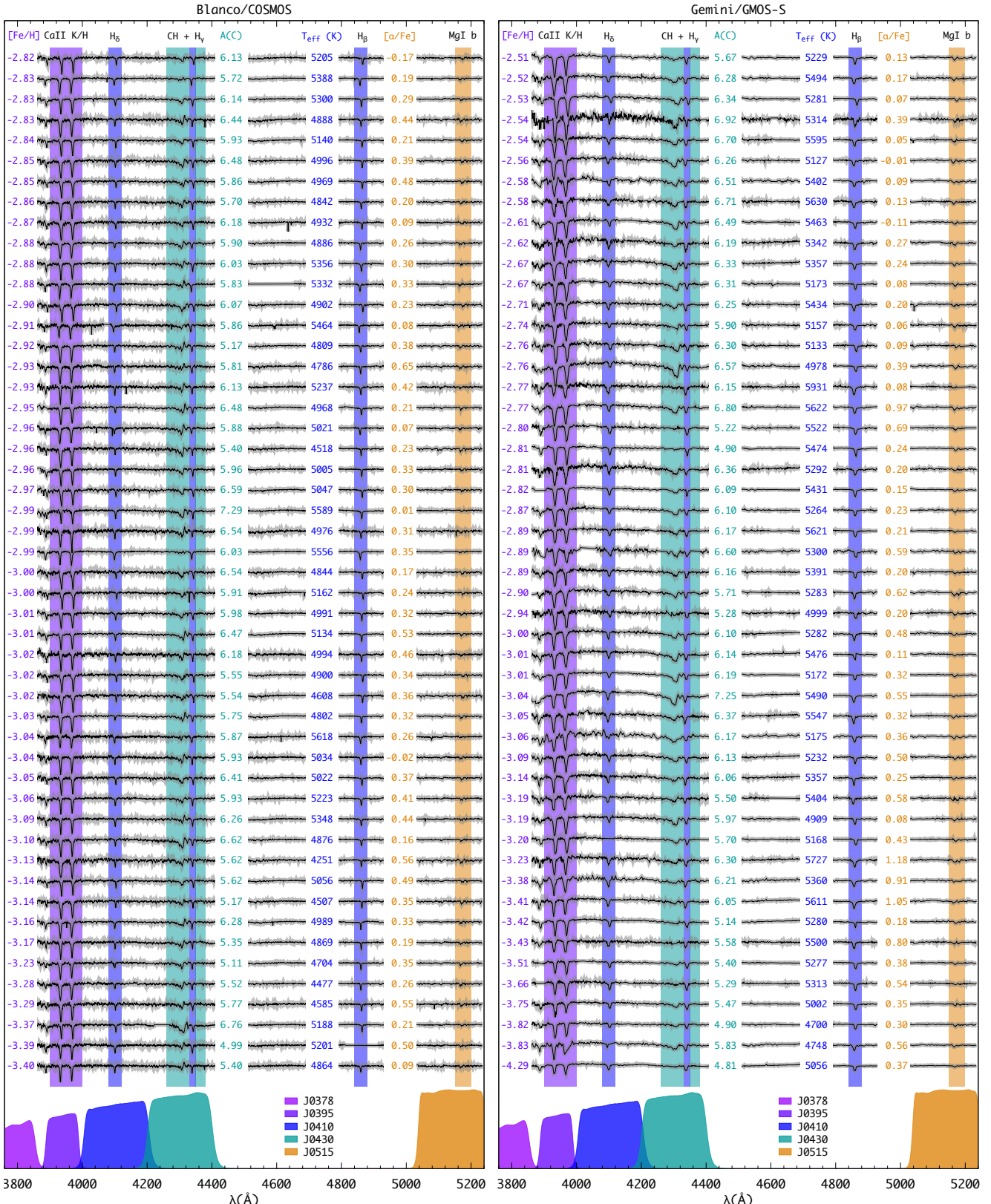


Figure 5. Example spectra for 100 program stars observed with Blanco (left panel) and Gemini-South (right panel), sorted by decreasing metallicity. The shaded areas highlight absorption features of interest for the determination of the stellar parameters and chemical abundances (see text for details). Also shown are the values calculated by the n-SSPP, as well as the S-PLUS filters that probe such features, with the exception of H_γ and H_β.

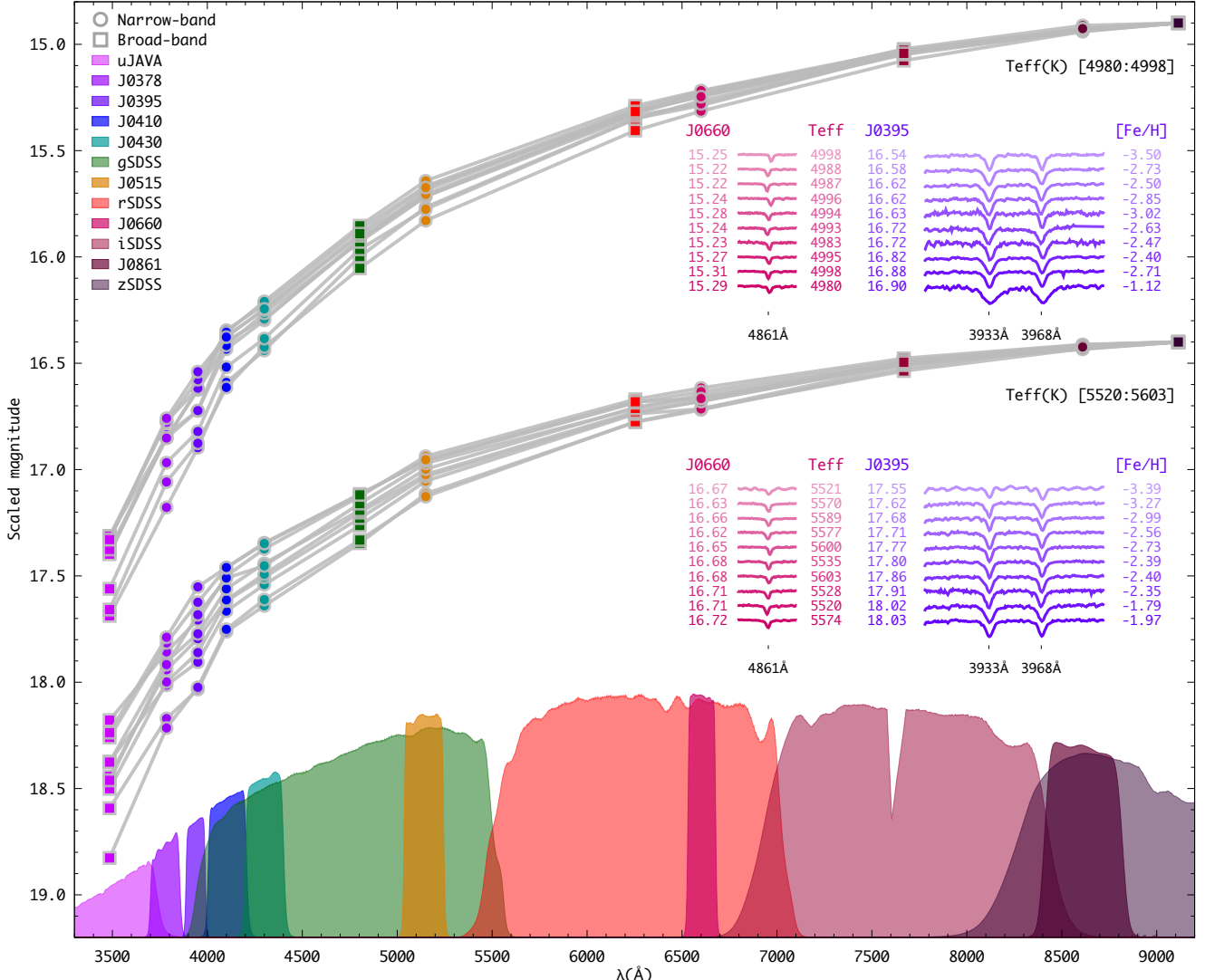


Figure 6. Spectral energy distribution (SED) for 20 selected program stars from Blanco and Gemini. Magnitudes were scaled to $z\text{SDSS}=14.9$ (top) and 16.4 (bottom). The temperature range for each set is displayed right below the SEDs. The insets show the observed spectra around the $\text{H}\beta$ and Ca II HK absorption features, sorted by their J0395 scaled magnitude. Also shown are the T_{eff} and $[\text{Fe}/\text{H}]$ for each star and the S-PLUS transmission curves. See text for further details.

their color indices and allow for a star-to-star comparison of the sensitivity of the other magnitudes to changes in stellar parameters. The insets show sections of the observed spectra (sorted by their J0395 scaled magnitude) around the Ca II HK and $\text{H}\beta$ features, as well as their respective parameters ($[\text{Fe}/\text{H}]$ and T_{eff}) and scaled magnitudes (J0395 and J0660). Assuming that the three bluest filters carry most of the metallicity information, it is possible to qualitatively see the larger variation in magnitudes, as compared with the magnitudes from the redder filters. Under the assumption that (most) of this variation is due to changes in metallicity, it is expected that the sorted J0395 magnitudes would naturally result in a $[\text{Fe}/\text{H}]$ sequence.

For the SEDs on the top set, all T_{eff} values are within 18 K, which translates into a 0.09 mag ($\sim 0.5\%$) variation in the J0660 flux. As expected, there is an increase of the J0395 magnitude with $[\text{Fe}/\text{H}]$. The two extremes of the $[\text{Fe}/\text{H}]$ scale have a 0.36 magnitude difference in J0395, which roughly translates into a 2.0 dex variation in $[\text{Fe}/\text{H}]$. At this temperature range, the above variation in the Ca II HK region flux is well above the typical magnitude uncertainties from S-PLUS, making it possible to have a good metallicity discriminant.

To a certain degree, the same applies to the bottom set of SEDs, which has an average T_{eff} about 500 K warmer than the top set, with a somewhat larger dispersion of 83 K. These warmer temperatures result in weaker ab-

sorption features when compared to the cooler set for a given [Fe/H], but are still larger than the typical uncertainties in the measured flux. For this group, the variation in the J0660 magnitude is very small (0.05 mag), while the difference between the extremes in J0395 (0.48 mag) still translates into a 1.5 dex range in terms of [Fe/H].

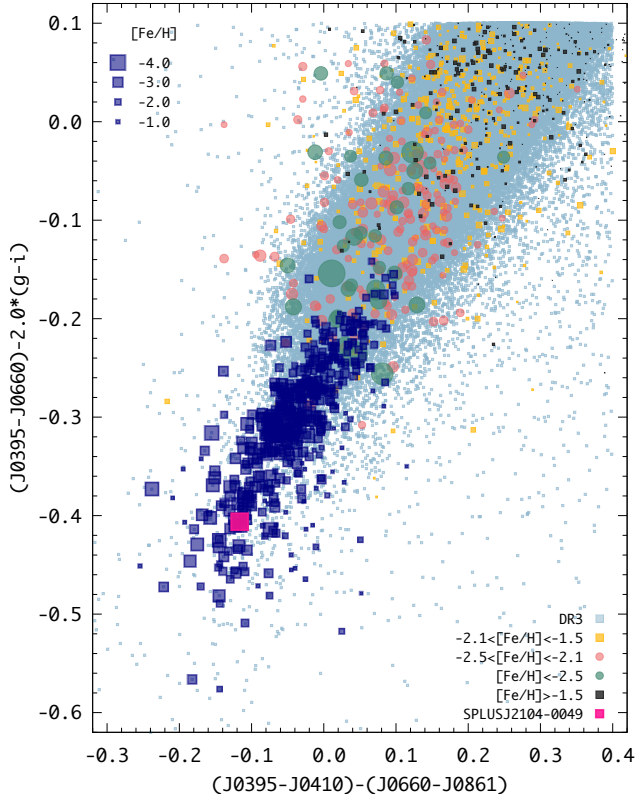


Figure 7. S-PLUS color-color diagram for DR3 (light blue filled squares), SDSS/SEGUE cross-match, and the stars observed in this work (dark blue filled squares). The point size is inversely proportional do the metallicity. Also shown is SPLUS J2104–0049, an ultra metal-poor star identified in S-PLUS.

4.2. Effectiveness of S-PLUS color selection

One of the main goals of this work is to improve the success rate of finding low-metallicity stars from photometry, taking advantage of the metallicity sensitivity of the S-PLUS narrow-band filters. Figure 7 shows the color-color diagram for the S-PLUS DR3 data, the cross-match between S-PLUS and SDSS/SEGUE (color-coded by metallicity range), and the 492 stars observed in this work. The point size is inversely proportional to [Fe/H]. The selection window for the spectroscopic follow-up, as defined in Section 2 is $(J0395-J0410)-(J0660-J0861) \in [-0.30:0.15]$ and

$(J0395-J0660)-2 \times (g-i) \in [-0.60:-0.15]$. Also shown in the figure is SPLUS J2104–0049, the first ultra metal-poor star identified in S-PLUS, with [Fe/H]=−4.03 (Placco et al. 2021).

There is, as expected, a strong correlation between metallicity and the position of a star in this color-color diagram. However, that does not imply a direct translation between these colors and [Fe/H], as evidenced by the stars with smaller points (higher metallicities) present towards negative colors. However, these higher-metallicity stars can be filtered-out by another color combination (see Section 4.4 below for further details). What still holds true, as set forth by Figure 2, is the fact that the fraction of stars with $[Fe/H] \leq -2.0$ increases for decreasing $(J0395-J0660)-2 \times (g-i)$ and $(J0395-J0410)-(J0660-J0861)$.

A different procedure to assess the efficiency of the color selection is by looking at the MDF of the observed stars and compare it with previous attempts of following-up low-metallicity star candidates. The top panel of Figure 8 shows the MDF of the stars observed in this work, compared with data from Placco et al. (2018), Placco et al. (2019), and Limberg et al. (2021)⁹ in the middle panels. The total number of stars and fractions for different metallicity ranges are also shown for each sample. The bottom panel shows the cumulative distribution function (CDF) for the three samples, indicating the 80th percentile value for [Fe/H]. It is possible to see that the S-PLUS color selection is far superior than the previous efforts in selecting low-metallicity star candidates. The success rate for $[Fe/H] \leq -2.0$ is $82^{+3\%}_{-4\%}{}^{10}$, as compared to 60% in Placco et al. (2018), 39% in Placco et al. (2019), and 30% in Limberg et al. (2021). Finally, the fraction of stars with $[Fe/H] \leq -3.0$ (14%) is higher than the fraction of stars with $[Fe/H] > -1.5$ (11%), which confirms the effectiveness of the S-PLUS color window in selecting low-metallicity stars.

4.3. Carbon and α -element abundances

The carbon and α -element abundances calculated by the n-SSPP can provide further insight on the origin of the observed stars and serve as selection criteria for high-resolution spectroscopic follow-up. Even though

⁹ Even though these two efforts have followed-up data selected from different approaches, both had the goal of maximizing the number of observed stars with $[Fe/H] \leq -2.0$. A comparison could also be made with the work of Aguado et al. (2019) and Da Costa et al. (2019). However, these studies used photometric metallicities for their target selection, as opposed to the color-color diagrams employed by this work.

¹⁰ Uncertainties in the fractions are represented by the Wilson score confidence intervals (Wilson 1927).

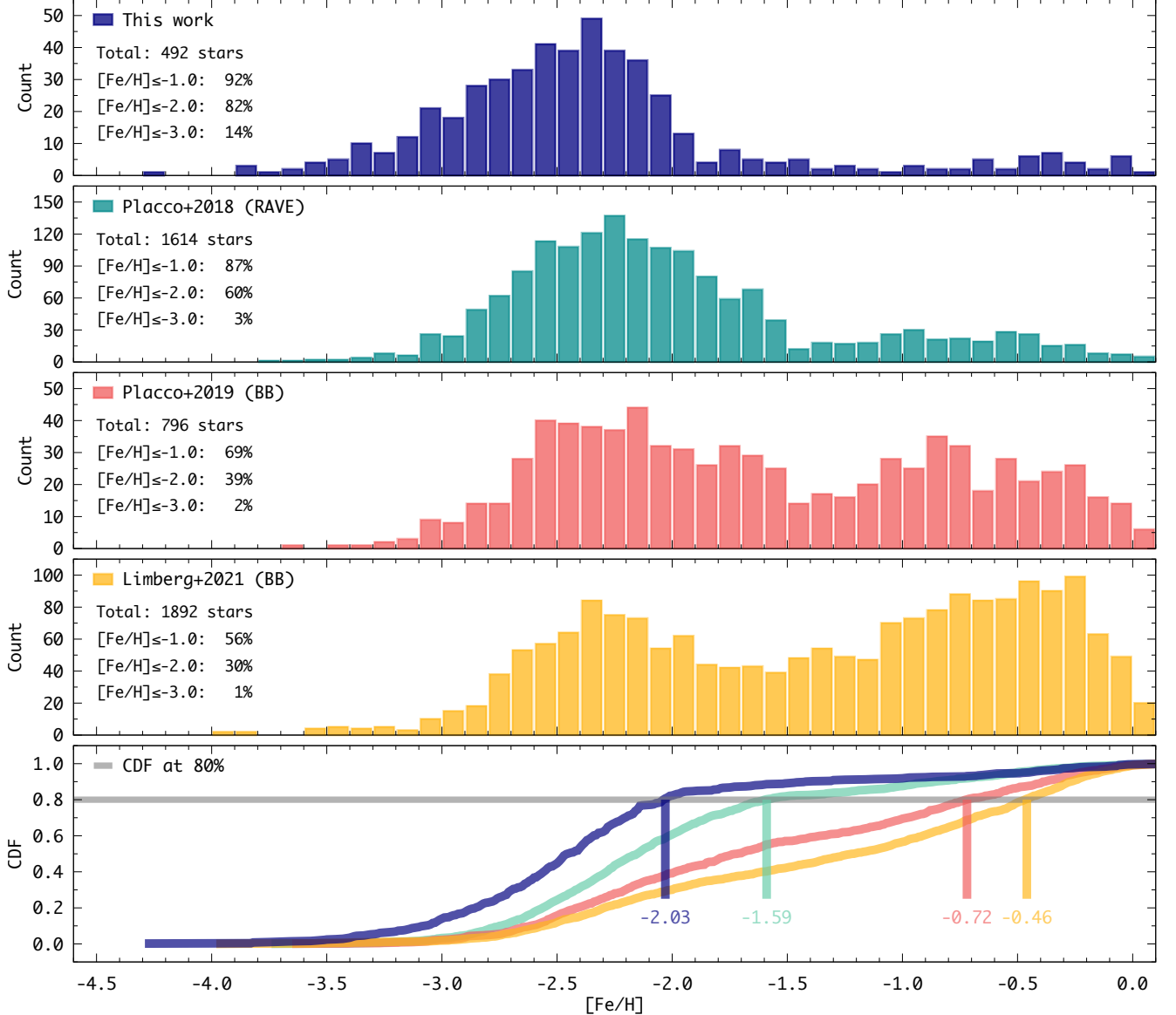


Figure 8. Metallicity histogram for the program stars (top panel), compared with the distributions from Placco et al. (2018), Placco et al. (2019), and Limberg et al. (2021) (middle panels). Each panel shows the total number of stars and the fractions for different metallicity regimes. The bottom panel shows the cumulative distribution functions (CDF) for the three samples, marking the $[\text{Fe}/\text{H}]$ value for which they reach 80%.

the carbon abundances in the SEGUE sample were not used for the target selection in this work, the $(g-i)$ color (and, to some extent, also the J0395 and J0395 magnitudes) are affected by the presence of carbon molecular bands in the spectrum. As a consequence of the decreased emerging flux on the g band, cool carbon-enhanced stars will fall outside the $(g-i)$ window defined in Section 2. Regardless, the abundances measured for the program stars allow for the calculation of the fractions of Carbon-Enhanced Metal-Poor (CEMP - $[\text{C}/\text{Fe}] \geq +0.7$; Aoki et al. 2007) stars as a function of the metallicity.

Figure 9 shows the distribution of $A(\text{C})$ (left panel) and $[\alpha/\text{Fe}]$ (right panel) for the sample stars as a function of the metallicity. The auxiliary panels show the marginal distributions. The lower left panel shows both the differential and cumulative CEMP fractions. Solid lines mark the solar values for the quantities, as well as the CEMP definition on the left panel and the average $[\alpha/\text{Fe}] = +0.4$ for the Galactic halo (Venn et al. 2004; Kobayashi et al. 2006) in the right panel. The point sizes are proportional to the temperature. The CEMP groups labeled are loosely defined based on the arguments presented in Yoon et al. (2016), which were built

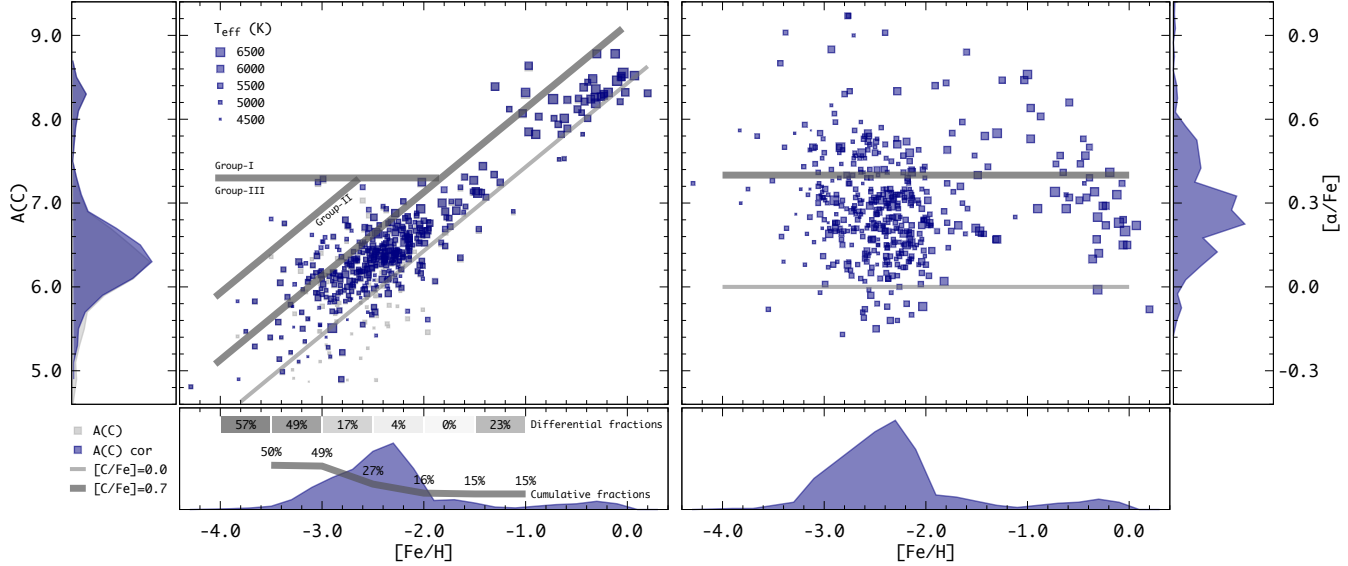


Figure 9. Absolute carbon, ($A(C)$), corrected as described in the text - left panel), and α -element abundance ratios, $[\alpha/Fe]$ (right panel), as a function of the metallicity calculated by the n-SSPP. The side and lower panels show the marginal distributions. The solid line in the lower left panel shows the cumulative CEMP fractions for the stars with $-3.5 \leq [Fe/H] \leq -1.0$ and the numbers of the top part of the panel are the differential fractions for 0.5 dex $[Fe/H]$ bins. Point sizes are proportional to T_{eff} .

upon the work of Spite et al. (2013); Bonifacio et al. (2015); Hansen et al. (2015). The average α -element abundance for the sample ($[\alpha/Fe] = +0.29$) is somewhat lower than the typical value for stars with $[Fe/H] < -2.0$ and there is no apparent trend with metallicities.

Stars in the CEMP Group-I are believed to have acquired their carbon in a binary system from a now-evolved companion that went through its AGB phase (extrinsic enrichment; Placco et al. 2014). Members of Groups-II and III, on the other hand, carry in their atmosphere the carbon signature inherited from its parent population (intrinsic enrichment). The distinction between Groups II and III lies on specific characteristics of the massive stars that polluted the gas clouds from which the subsequent low-mass stars were formed. For the sample presented in this work, there are 59 CEMP stars, with 4 stars in Group-I, 51 in Group-II, and 4 in Group-III. Compared with the work of Yoon et al. (2016), the sample presented in this work has an exceptionally low number of Group-I stars, which should be the majority in the CEMP population. This may be a direct consequence of the ($g-i$) cut mentioned above, which would exclude most of the higher metallicity and higher carbon abundance stars associated with the Group-I.

The cumulative CEMP fractions showed in the lower panel of Figure 9 are consistently lower for $[Fe/H] < -1.0$ and < -2.0 when compared to other empirical estimates in the literature, derived from samples with similar spectral resolution (Placco et al. 2018; Yoon et al. 2018;

Placco et al. 2019; Limberg et al. 2021). This may be, once more, a consequence of the selection methods employed in this work. The same applies to the differential fractions. The fractions are in better agreement for the $[Fe/H] < -3.0$ regime, which could be due to the fact that Group-III stars dominate the CEMP population in this metallicity regime (see Arentsen et al. 2022, for a complete review of the CEMP fractions in the literature).

4.4. Further improvements in the color selection

Even though the S-PLUS color selections presented in this work are effective in selecting low-metallicity stars, additional restrictions can be made in order to decrease the number of stars with $[Fe/H] \geq -1.0$ for further spectroscopic follow-up and targeting. Further inspection of Figure 4 reveals that 43% of the stars with $T_{eff} \geq 5900$ K have $[Fe/H] \geq -1.0$, while only 3% of the stars with $T_{eff} < 5900$ K have $[Fe/H] \geq -1.0$.

An exploratory analysis was conducted to search for an additional S-PLUS color combination that would help remove the higher metallicity stars for the continuation of the spectroscopic follow-up. One such candidate is (J0378-i)-(J0410-J0660), which contains the metallicity-sensitive J0378 filter and the temperature-sensitive (J0410-J0660) color index. The top panel of Figure 10 shows the behavior of this color as a function of the metallicity. It is possible to see a very strong correlation between the two quantities, and a tentative cut was made at (J0378-i)-(J0410-J0660)=0.80. The

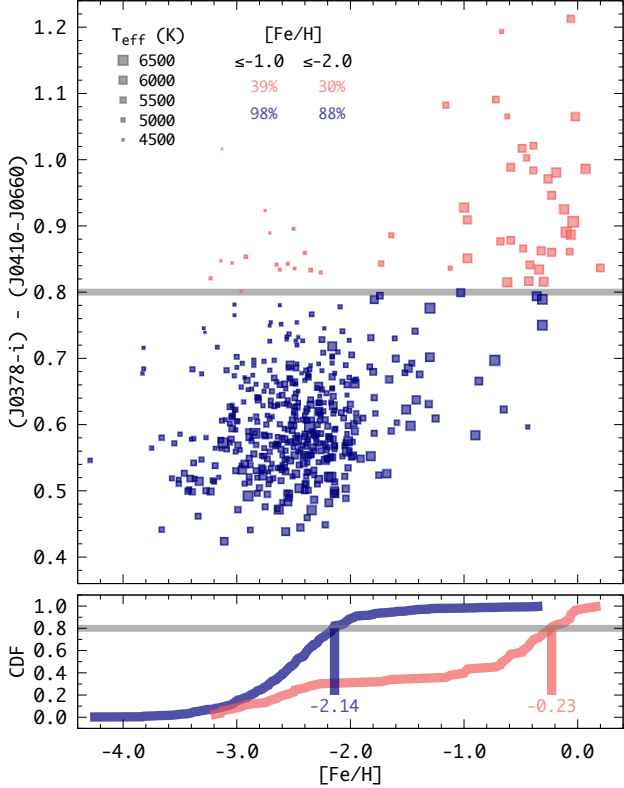


Figure 10. Top panel: $(J0378-i)-(J0410-J0660)$ as a function of the metallicity for the observed sample, with the gray line marking the proposed color cut. Also shown are the fractions of stars with $[Fe/H] \leq -1.0$ and ≤ -2.0 for the two subsamples. The point sizes are proportional to T_{eff} . Bottom panel: cumulative distribution functions (CDF) for the two subsamples, marking the $[Fe/H]$ value for which they reach 80%.

high color index subsample (red points) is dominated by the higher metallicity stars, with only 30% of the stars with $[Fe/H] \leq -1.0$ and 39% with $[Fe/H] \leq -2.0$. For the low color index subsample (blue points), the fractions are 98% for stars with $[Fe/H] \leq -1.0$ and 88% with $[Fe/H] \leq -2.0$. The bottom panel shows the CDFs for both subsamples, indicating the 80th percentile value for $[Fe/H]$.

This additional color restriction further improves the success rate for the identification of stars with $[Fe/H] \leq -2.0$ from the S-PLUS photometry. Even though there are low-metallicity stars with $(J0378-i)-(J0410-J0660) > 0.8$, their fraction is substantially smaller than for $(J0378-i)-(J0410-J0660) < 0.8$. The stars at the high color index subsample with $[Fe/H] \leq -2.0$ are all low-temperature ($T_{\text{eff}} \lesssim 4800$ K) and low-carbon ($[C/Fe] \leq 0.0$).

606

5. CONCLUSIONS

This work presented the medium-resolution spectroscopic follow-up of 492 low-metallicity star candidates selected from their S-PLUS photometry. By using metallicity-sensitive colors, the success rate found is 92 $^{+2}_{-3}\%$ for $[Fe/H] \leq -1.0$, 82 $^{+3}_{-4}\%$ for $[Fe/H] \leq -2.0$, and 14 $^{+3}_{-3}\%$ for $[Fe/H] \leq -3.0$, including one ultra metal-poor star ($[Fe/H] \leq -4.0$). Based on the carbonicity determinations, there are 59 CEMP stars in the sample, including 51 Group-II and 4 Group-III. Most of these are already being followed-up with high-resolution spectroscopy in order to determine their chemical abundance pattern and further understand their origin. Based on the $[Fe/H]$ determined in this work, a further color restriction is proposed, which can potentially increase the fractions of stars with $[Fe/H] \leq -1.0$ and ≤ -2.0 to 98% and 88%, respectively.

The unpretentious color selection described in this work is not only extremely effective in providing targets for further spectroscopic studies, but also establishes a framework in which upcoming fiber-fed multiplex surveys can benefit from in terms of targeting. These surveys will continue to provide the individual pieces that constitute the cosmic puzzle that is the chemical evolution of the universe.

The work of V.M.P. is supported by NOIRLab, which is managed by the Association of Universities for Research in Astronomy (AURA) under a cooperative agreement with the National Science Foundation. F.A.-F. acknowledges funding for this work from FAPESP grants 2018/20977-2 and 2021/09468-1. A.A. gratefully acknowledges funding from the European Research Council (ERC) under the European Unions Horizon 2020 research and innovation programme (grant agreement No. 834148). Y.S.L. acknowledges support from the National Research Foundation (NRF) of Korea grant funded by the Ministry of Science and ICT (NRF-2021R1A2C1008679). The S-PLUS project, including the T80-South robotic telescope and the S-PLUS scientific survey, was founded as a partnership between the Fundação de Amparo à Pesquisa do Estado de São Paulo (FAPESP), the Observatório Nacional (ON), the Federal University of Sergipe (UFS), and the Federal University of Santa Catarina (UFSC), with important financial and practical contributions from other collaborating institutes in Brazil, Chile (Universidad de La Serena), and Spain (Centro de Estudios de Física del Cosmos de Aragón, CEFCA). We further acknowledge financial support from the São Paulo Research

655 Foundation (FAPESP), the Brazilian National Research
656 Council (CNPq), the Coordination for the Improvement
657 of Higher Education Personnel (CAPES), the Carlos
658 Chagas Filho Rio de Janeiro State Research Founda-
659 tion (FAPERJ), and the Brazilian Innovation Agency
660 (FINEP). The members of the S-PLUS collaboration are
661 grateful for the contributions from CTIO staff in helping
662 in the construction, commissioning and maintenance of
663 the T80-South telescope and camera. We are also in-
664 debted to Rene Laporte, INPE, and Keith Taylor for
665 their important contributions to the project. From CE-
666 FCA, we thank Antonio Marín-Franch for his invaluable
667 contributions in the early phases of the project, David
668 Cristóbal-Hornillos and his team for their help with the
669 installation of the data reduction package JYPE version
670 0.9.9, César Íñiguez for providing 2D measurements of
671 the filter transmissions, and all other staff members for
672 their support with various aspects of the project. Based
673 on observations made at Cerro Tololo Inter-American
674 Observatory at NSF's NOIRLab (NOIRLab Prop. IDs
675 2019B-0069, 2020A-0032, 2022A-210002; PI: V. Placco),
676 which is managed by the Association of Universities for
677 Research in Astronomy (AURA) under a cooperative
678 agreement with the National Science Foundation. Based
679 on observations obtained at the international Gemini
680 Observatory (Program IDs: GS-2019A-Q-408, GS-
681 2021A-Q-419), a program of NSF's NOIRLab, which is
682 managed by the Association of Universities for Research
683 in Astronomy (AURA) under a cooperative agreement
684 with the National Science Foundation. on behalf of the
685 Gemini Observatory partnership: the National Science
686 Foundation (United States), National Research Council
687 (Canada), Agencia Nacional de Investigación y Desar-
688 rollo (Chile), Ministerio de Ciencia, Tecnología e Inno-
689 vación (Argentina), Ministério da Ciência, Tecnologia,
690 Inovações e Comunicações (Brazil), and Korea Astron-
691 omy and Space Science Institute (Republic of Korea).
692 This research has made use of NASA's Astrophysics
693 Data System Bibliographic Services; the arXiv pre-print
694 server operated by Cornell University; the SIMBAD
695 database hosted by the Strasbourg Astronomical Data
696 Center; and the online Q&A platform **stackoverflow**
697 (<http://stackoverflow.com/>).

698 *Software:* `awk` (Aho et al. 1987), `dustmaps` (Green
699 2018), `DRAGONS` (Labrie et al. 2019), `gnuplot` (Williams
700 & Kelley 2015), `IRAF` (Tody 1986, 1993),
701 `matplotlib` (Hunter 2007), `n-SSPP` (Beers et al. 2014),
702 `numpy` (Oliphant 2006), `pandas` (McKinney 2010),
703 `sed` (McMahon 1979), `stilts` (Taylor 2006).

704 *Facilities:* Blanco (COSMOS), Gemini:South
705 (GMOS)

REFERENCES

- 706 Aguado, D. S., Youakim, K., González Hernández, J. I.,
 707 et al. 2019, MNRAS, 490, 2241,
 708 doi: [10.1093/mnras/stz2643](https://doi.org/10.1093/mnras/stz2643)
- 709 Aho, A. V., Kernighan, B. W., & Weinberger, P. J. 1987,
 710 The AWK Programming Language (Boston, MA, USA:
 711 Addison-Wesley Longman Publishing Co., Inc.)
- 712 Allende Prieto, C. 2016, A&A, 595, A129,
 713 doi: [10.1051/0004-6361/201628789](https://doi.org/10.1051/0004-6361/201628789)
- 714 Almeida-Fernandes, F., SamPedro, L., Herpich, F. R., et al.
 715 2022, MNRAS, 511, 4590, doi: [10.1093/mnras/stac284](https://doi.org/10.1093/mnras/stac284)
- 716 Alonso, A., Arribas, S., & Martínez-Roger, C. 1996, A&A,
 717 313, 873
- 718 Alonso, A., Arribas, S., & Martínez-Roger, C. 1999, A&AS,
 719 140, 261, doi: [10.1051/aas:1999521](https://doi.org/10.1051/aas:1999521)
- 720 An, D., Beers, T. C., Santucci, R. M., et al. 2015, ApJL,
 721 813, L28, doi: [10.1088/2041-8205/813/2/L28](https://doi.org/10.1088/2041-8205/813/2/L28)
- 722 An, D., Beers, T. C., Johnson, J. A., et al. 2013, ApJ, 763,
 723 65, doi: [10.1088/0004-637X/763/1/65](https://doi.org/10.1088/0004-637X/763/1/65)
- 724 Andrés Galarza, C., Daflon, S., Placco, V. M., et al. 2021,
 725 arXiv e-prints, arXiv:2109.11600.
<https://arxiv.org/abs/2109.11600>
- 726 Aoki, W., Beers, T. C., Christlieb, N., et al. 2007, ApJ,
 727 655, 492, doi: [10.1086/509817](https://doi.org/10.1086/509817)
- 728 Arentsen, A., Placco, V. M., Lee, Y. S., et al. 2022, A&A –
 729 in preparation
- 730 Beers, T. C., & Christlieb, N. 2005, ARA&A, 43, 531
- 731 Beers, T. C., Norris, J. E., Placco, V. M., et al. 2014, ApJ,
 732 794, 58, doi: [10.1088/0004-637X/794/1/58](https://doi.org/10.1088/0004-637X/794/1/58)
- 733 Beers, T. C., Placco, V. M., Carollo, D., et al. 2017, ApJ,
 734 835, 81, doi: [10.3847/1538-4357/835/1/81](https://doi.org/10.3847/1538-4357/835/1/81)
- 735 Bessell, M., Bloxham, G., Schmidt, B., et al. 2011, PASP,
 736 123, 789, doi: [10.1086/660849](https://doi.org/10.1086/660849)
- 737 Bessell, M. S. 1979, PASP, 91, 589, doi: [10.1086/130542](https://doi.org/10.1086/130542)
- 738 Bonifacio, P., Monai, S., & Beers, T. C. 2000, AJ, 120,
 739 2065, doi: [10.1086/301566](https://doi.org/10.1086/301566)
- 740 Bonifacio, P., Caffau, E., Spite, M., et al. 2015, A&A, 579,
 741 A28, doi: [10.1051/0004-6361/201425266](https://doi.org/10.1051/0004-6361/201425266)
- 742 Bromm, V., & Larson, R. B. 2004, ARA&A, 42, 79,
 743 doi: [10.1146/annurev.astro.42.053102.134034](https://doi.org/10.1146/annurev.astro.42.053102.134034)
- 744 Carney, B. W., & Peterson, R. C. 1981, ApJ, 245, 238,
 745 doi: [10.1086/158804](https://doi.org/10.1086/158804)
- 746 Casagrande, L., Ramírez, I., Meléndez, J., Bessell, M., &
 747 Asplund, M. 2010, A&A, 512, A54,
 748 doi: [10.1051/0004-6361/200913204](https://doi.org/10.1051/0004-6361/200913204)
- 749 Casagrande, L., Wolf, C., Mackey, A. D., et al. 2019,
 750 MNRAS, 482, 2770, doi: [10.1093/mnras/sty2878](https://doi.org/10.1093/mnras/sty2878)
- 751 Cenarro, A. J., Moles, M., Cristóbal-Hornillos, D., et al.
 752 2019, A&A, 622, A176,
 753 doi: [10.1051/0004-6361/201833036](https://doi.org/10.1051/0004-6361/201833036)
- 755 Chitti, A., Frebel, A., Mardini, M. K., et al. 2021a, ApJS,
 756 254, 31, doi: [10.3847/1538-4365/abf73d](https://doi.org/10.3847/1538-4365/abf73d)
- 757 Chitti, A., Mardini, M. K., Frebel, A., & Daniel, T. 2021b,
 758 ApJL, 911, L23, doi: [10.3847/2041-8213/abd629](https://doi.org/10.3847/2041-8213/abd629)
- 759 Da Costa, G. S., Bessell, M. S., Mackey, A. D., et al. 2019,
 760 MNRAS, 489, 5900, doi: [10.1093/mnras/stz2550](https://doi.org/10.1093/mnras/stz2550)
- 761 Davies, R. L., Allington-Smith, J. R., Bettess, P., et al.
 762 1997, in Proc. SPIE, Vol. 2871, Optical Telescopes of
 763 Today and Tomorrow, ed. A. L. Ardeberg, 1099–1106,
 764 doi: [10.1117/12.268996](https://doi.org/10.1117/12.268996)
- 765 Demarque, P., Woo, J.-H., Kim, Y.-C., & Yi, S. K. 2004,
 766 ApJS, 155, 667, doi: [10.1086/424966](https://doi.org/10.1086/424966)
- 767 Dotter, A., Chaboyer, B., Jevremović, D., et al. 2008,
 768 ApJS, 178, 89, doi: [10.1086/589654](https://doi.org/10.1086/589654)
- 769 Frebel, A., & Norris, J. E. 2015, ARA&A, 53, 631,
 770 doi: [10.1146/annurev-astro-082214-122423](https://doi.org/10.1146/annurev-astro-082214-122423)
- 771 Fukugita, M., Ichikawa, T., Gunn, J. E., et al. 1996, AJ,
 772 111, 1748, doi: [10.1086/117915](https://doi.org/10.1086/117915)
- 773 Gimeno, G., Roth, K., Chiboucas, K., et al. 2016, in
 774 Proc. SPIE, Vol. 9908, Ground-based and Airborne
 775 Instrumentation for Astronomy VI, 99082S,
 776 doi: [10.1117/12.2233883](https://doi.org/10.1117/12.2233883)
- 777 Greaves, W. M. H., Davidson, C., & Martin, E. 1929,
 778 MNRAS, 90, 104, doi: [10.1093/mnras/90.1.104](https://doi.org/10.1093/mnras/90.1.104)
- 779 Green, G. 2018, The Journal of Open Source Software, 3,
 780 695, doi: [10.21105/joss.00695](https://doi.org/10.21105/joss.00695)
- 781 Hansen, T., Hansen, C. J., Christlieb, N., et al. 2015, ApJ,
 782 807, 173, doi: [10.1088/0004-637X/807/2/173](https://doi.org/10.1088/0004-637X/807/2/173)
- 783 Heger, A., & Woosley, S. E. 2002, ApJ, 567, 532,
 784 doi: [10.1086/338487](https://doi.org/10.1086/338487)
- 785 Huang, Y., Chen, B. Q., Yuan, H. B., et al. 2019, ApJS,
 786 243, 7, doi: [10.3847/1538-4365/ab1f72](https://doi.org/10.3847/1538-4365/ab1f72)
- 787 Hunter, J. D. 2007, Computing in Science & Engineering, 9,
 788 90, doi: [10.1109/MCSE.2007.55](https://doi.org/10.1109/MCSE.2007.55)
- 789 Ivezić, Ž., Sesar, B., Jurić, M., et al. 2008, ApJ, 684, 287,
 790 doi: [10.1086/589678](https://doi.org/10.1086/589678)
- 791 Keller, S. C., Schmidt, B. P., Bessell, M. S., et al. 2007,
 792 PASA, 24, 1, doi: [10.1071/AS07001](https://doi.org/10.1071/AS07001)
- 793 Kobayashi, C., Umeda, H., Nomoto, K., Tominaga, N., &
 794 Ohkubo, T. 2006, ApJ, 653, 1145, doi: [10.1086/508914](https://doi.org/10.1086/508914)
- 795 Labrie, K., Anderson, K., Cárdenes, R., Simpson, C., &
 796 Turner, J. E. H. 2019, in Astronomical Society of the
 797 Pacific Conference Series, Vol. 523, Astronomical Data
 798 Analysis Software and Systems XXVII, ed. P. J. Teuben,
 799 M. W. Pound, B. A. Thomas, & E. M. Warner, 321
- 800 Lee, Y. S., Beers, T. C., Sivarani, T., et al. 2008a, AJ, 136,
 801 2022, doi: [10.1088/0004-6256/136/5/2022](https://doi.org/10.1088/0004-6256/136/5/2022)
- 802 —. 2008b, AJ, 136, 2050,
 803 doi: [10.1088/0004-6256/136/5/2050](https://doi.org/10.1088/0004-6256/136/5/2050)

- 804 Lee, Y. S., Beers, T. C., Allende Prieto, C., et al. 2011, AJ, 141, 90, doi: [10.1088/0004-6256/141/3/90](https://doi.org/10.1088/0004-6256/141/3/90)
- 805 Lee, Y. S., Beers, T. C., Masseron, T., et al. 2013, AJ, 146, 132, doi: [10.1088/0004-6256/146/5/132](https://doi.org/10.1088/0004-6256/146/5/132)
- 806 Leggett, S. K., Birmingham, B., Saumon, D., et al. 2010, ApJ, 710, 1627, doi: [10.1088/0004-637X/710/2/1627](https://doi.org/10.1088/0004-637X/710/2/1627)
- 807 Limberg, G., Santucci, R. M., Rossi, S., et al. 2021, ApJ, 913, 11, doi: [10.3847/1538-4357/abeefe](https://doi.org/10.3847/1538-4357/abeefe)
- 808 Lucatello, S., Beers, T. C., Christlieb, N., et al. 2006, ApJL, 652, L37, doi: [10.1086/509780](https://doi.org/10.1086/509780)
- 809 Majewski, S. R., Ostheimer, J. C., Kunkel, W. E., & Patterson, R. J. 2000, AJ, 120, 2550, doi: [10.1086/316836](https://doi.org/10.1086/316836)
- 810 Martini, P., Elias, J., Points, S., et al. 2014, in Proc. SPIE, Vol. 9147, Ground-based and Airborne Instrumentation for Astronomy V, 91470Z, doi: [10.1117/12.2056834](https://doi.org/10.1117/12.2056834)
- 811 Masseron, T., Johnson, J. A., Plez, B., et al. 2010, A&A, 509, A93+, doi: [10.1051/0004-6361/200911744](https://doi.org/10.1051/0004-6361/200911744)
- 812 McKinney, W. 2010, in Proceedings of the 9th Python in Science Conference, ed. S. van der Walt & J. Millman, 51 – 56
- 813 Mcmahon, L. E. 1979, in UNIX Programmer’s Manual - 7th Edition, volume 2, Bell Telephone Laboratories (Murray Hill)
- 814 Mendes de Oliveira, C., Ribeiro, T., Schoenell, W., et al. 2019, MNRAS, 489, 241, doi: [10.1093/mnras/stz1985](https://doi.org/10.1093/mnras/stz1985)
- 815 Meynet, G., Ekström, S., & Maeder, A. 2006, A&A, 447, 623, doi: [10.1051/0004-6361:20053070](https://doi.org/10.1051/0004-6361:20053070)
- 816 Molino, A., Costa-Duarte, M. V., Sampedro, L., et al. 2019, arXiv e-prints, arXiv:1907.06315.
<https://arxiv.org/abs/1907.06315>
- 817 Norris, J. E., Bessell, M. S., Yong, D., et al. 2013, ApJ, 762, 25, doi: [10.1088/0004-637X/762/1/25](https://doi.org/10.1088/0004-637X/762/1/25)
- 818 Oliphant, T. E. 2006, A guide to NumPy, Vol. 1 (Trelgol Publishing USA)
- 819 Placco, V. M., Frebel, A., Beers, T. C., & Stancliffe, R. J. 2014, ApJ, 797, 21, doi: [10.1088/0004-637X/797/1/21](https://doi.org/10.1088/0004-637X/797/1/21)
- 820 Placco, V. M., Beers, T. C., Santucci, R. M., et al. 2018, AJ, 155, 256, doi: [10.3847/1538-3881/aac20c](https://doi.org/10.3847/1538-3881/aac20c)
- 821 Placco, V. M., Santucci, R. M., Beers, T. C., et al. 2019, ApJ, 870, 122, doi: [10.3847/1538-4357/aaf3b9](https://doi.org/10.3847/1538-4357/aaf3b9)
- 822 Placco, V. M., Roederer, I. U., Lee, Y. S., et al. 2021, ApJL, 912, L32, doi: [10.3847/2041-8213/abf93d](https://doi.org/10.3847/2041-8213/abf93d)
- 823 Rockosi, C. M., Lee, Y. S., Morrison, H. L., et al. 2022, ApJS, 259, 60, doi: [10.3847/1538-4365/ac5323](https://doi.org/10.3847/1538-4365/ac5323)
- 824 Schlegel, D. J., Finkbeiner, D. P., & Davis, M. 1998, ApJ, 500, 525, doi: [10.1086/305772](https://doi.org/10.1086/305772)
- 825 Schuster, W. J., & Nissen, P. E. 1989, A&A, 221, 65
- 826 Spite, M., Caffau, E., Bonifacio, P., et al. 2013, A&A, 552, A107, doi: [10.1051/0004-6361/201220989](https://doi.org/10.1051/0004-6361/201220989)
- 827 Starkenburg, E., Martin, N., Youakim, K., et al. 2017, MNRAS, 471, 2587, doi: [10.1093/mnras/stx1068](https://doi.org/10.1093/mnras/stx1068)
- 828 Taylor, M. B. 2006, in Astronomical Society of the Pacific Conference Series, Vol. 351, Astronomical Data Analysis Software and Systems XV, ed. C. Gabriel, C. Arviset, D. Ponz, & S. Enrique, 666
- 829 Tody, D. 1986, in Proc. SPIE, Vol. 627, Instrumentation in astronomy VI, ed. D. L. Crawford, 733, doi: [10.1117/12.968154](https://doi.org/10.1117/12.968154)
- 830 Tody, D. 1993, in Astronomical Society of the Pacific Conference Series, Vol. 52, Astronomical Data Analysis Software and Systems II, ed. R. J. Hanisch, R. J. V. Brissenden, & J. Barnes, 173
- 831 Venn, K. A., Irwin, M., Shetrone, M. D., et al. 2004, AJ, 128, 1177, doi: [10.1086/422734](https://doi.org/10.1086/422734)
- 832 Wallerstein, G. 1964, PASP, 76, 175, doi: [10.1086/128079](https://doi.org/10.1086/128079)
- 833 Whitten, D. D., Placco, V. M., Beers, T. C., et al. 2019, A&A, 622, A182, doi: [10.1051/0004-6361/201833368](https://doi.org/10.1051/0004-6361/201833368)
- 834 —. 2021, ApJ, 912, 147, doi: [10.3847/1538-4357/abee7e](https://doi.org/10.3847/1538-4357/abee7e)
- 835 Williams, T., & Kelley, C. 2015, Gnuplot 5.0: an interactive plotting program, <http://www.gnuplot.info/>
- 836 Wilson, E. B. 1927, Journal of the American Statistical Association, 22, 209, doi: [10.1080/01621459.1927.10502953](https://doi.org/10.1080/01621459.1927.10502953)
- 837 Wolf, C., Onken, C. A., Luval, L. C., et al. 2018, PASA, 35, e010, doi: [10.1017/pasa.2018.5](https://doi.org/10.1017/pasa.2018.5)
- 838 Woosley, S. E., & Weaver, T. A. 1995, ApJS, 101, 181, doi: [10.1086/192237](https://doi.org/10.1086/192237)
- 839 Yanny, B., Rockosi, C., Newberg, H. J., et al. 2009, AJ, 137, 4377, doi: [10.1088/0004-6256/137/5/4377](https://doi.org/10.1088/0004-6256/137/5/4377)
- 840 Yoon, J., Beers, T. C., Placco, V. M., et al. 2016, ApJ, 833, 20, doi: [10.3847/0004-637X/833/1/20](https://doi.org/10.3847/0004-637X/833/1/20)
- 841 Yoon, J., Beers, T. C., Dietz, S., et al. 2018, ApJ, 861, 146, doi: [10.3847/1538-4357/aaccea](https://doi.org/10.3847/1538-4357/aaccea)
- 842 York, D. G., Adelman, J., Anderson, Jr., J. E., et al. 2000, AJ, 120, 1579, doi: [10.1086/301513](https://doi.org/10.1086/301513)
- 843 Youakim, K., Starkenburg, E., Aguado, D. S., et al. 2017, MNRAS, 472, 2963, doi: [10.1093/mnras/stx2005](https://doi.org/10.1093/mnras/stx2005)

Table 1. Observing Details

Star Name (2MASS)	α (J2000)	δ (J2000)	l (deg)	b (deg)	Date (UTC)	Telescope	Instrument	Proposal ID	Exp. (s)
----------------------	---------------------	---------------------	--------------	--------------	---------------	-----------	------------	-------------	-------------

Table 2. S-PLUS Photometry

Star Name	uJAVA	σ	J0378	σ	J0395	σ	J0410	σ	J0430	σ	gSDSS	σ	J0515	σ	rSDSS	σ	J0660	σ	iSDSS	σ	J0861	σ	zSDSS	σ
-----------	-------	----------	-------	----------	-------	----------	-------	----------	-------	----------	-------	----------	-------	----------	-------	----------	-------	----------	-------	----------	-------	----------	-------	----------

Table 3. Stellar Parameters and Abundances from the n-SSPP

Star Name (2MASS)	T_{eff} (K)	$\log g$ (cgs)	[Fe/H]	[C/Fe]	$\Delta [\text{C}/\text{Fe}]$	a	b	$A(\text{C})_{\text{cor}}$	c	$[\alpha/\text{Fe}]$

^a Carbon correction from [Placco et al. \(2014\)](#).^b Corrected carbon-to-iron ratio.^c Corrected absolute carbon abundance.